5Ni/MgO and 5Ni/MgO + MO$_x$ (M = Zr, Ti, Al) Catalyst for Hydrogen Production via Dry Reforming of Methane: Promotor-Free, Cost-Effective, and Handy Catalyst System

Naitik Patel[1] · Ahmed S. Al-Fatesh[2] · Nouf A. Bamatraf[3] · Ahmed I. Osman[4] · Salwa B. Alreshaidan[3] · Anis H. Fakeeha[2] · Irfan Wazeer[2] · Rawesh Kumar[1]

Abstract

Utilization of CO_2 as a promising oxidant under dry reforming methane (DRM) can mitigate two greenhouse gases (CO_2 and CH_4) together, as well as DRM reaction may be a source of H_2 energy in future. The cost-effective and handy catalyst preparation procedures like mixing, drying and calcining may turn this reaction from lab to industry. In this line, herein, 5Ni/MgO and 5Ni/MgO + MO$_x$ (M = Zr, Ti, Al) catalysts were prepared, investigated for DRM and characterized by X-ray diffraction, Raman, temperature programmed reduction/desorption, thermogravimetry and transmission electron microscope. Among the prepared catalysts, the 5Ni/MgO + TiO$_2$ catalyst exhibits the highest concentration of active Ni sites enhanced reducibility under oxidizing and reducing environments, but catalytic excellency is hindered by severe graphitic-type coke deposition. On the other hand, the 5Ni/MgO + Al$_2$O$_3$ catalyst predominantly comprises metallic Ni resulting from the reduction of "strongly interacted NiO", expanded surface area and the highest concentration of easily accessible active sites, contributing to its superior performance (H_2 yield ~ 71% up to 430 min time on stream) under oxidizing and reducing conditions during DRM. The outstanding performance of the 5Ni/MgO + Al$_2$O$_3$ catalyst marks a significant stride towards the development of an industrially viable, cost-effective, and convenient catalyst system for DRM.

✉ Ahmed S. Al-Fatesh
aalfatesh@ksu.edu.sa

✉ Ahmed I. Osman
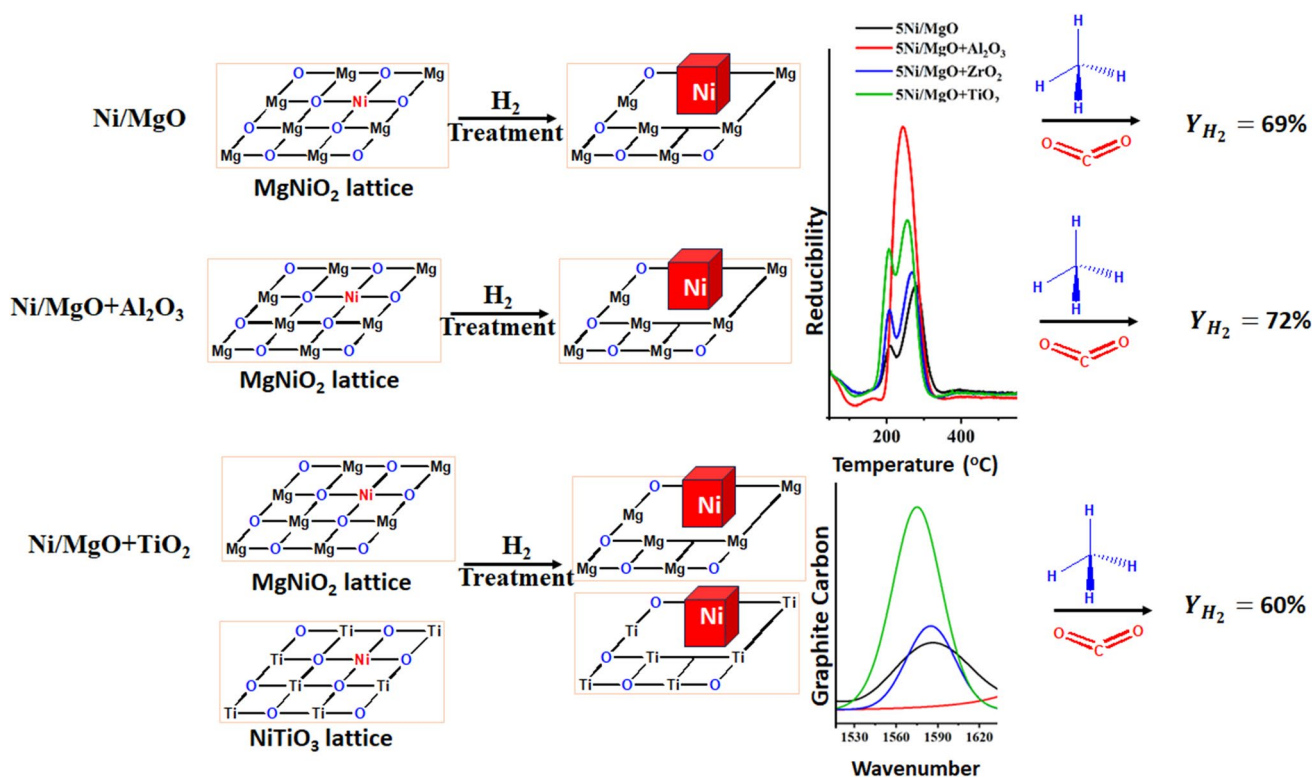aosmanahmed01@qub.ac.uk

✉ Rawesh Kumar
kr.rawesh@gmail.com

1 Department of Chemistry, Indus University, Ahmedabad, Gujarat 382115, India

2 Chemical Engineering Department, College of Engineering, King Saud University, P.O. Box 800, 11421 Riyadh, Saudi Arabia

3 Department of Chemistry, Faculty of Science, King Saud University, P.O. Box 800, 11451 Riyadh, Saudi Arabia

4 School of Chemistry and Chemical Engineering, Queen's University Belfast, Belfast, Northern Ireland BT9 5AG, UK

Graphical Abstract

1 Introduction

Global warming continues to drive the scientific community towards catalytic solutions aimed at converting greenhouse gases into non-greenhouse gases. In this endeavor, the process of dry reforming of methane (DRM) emerges as a particularly insightful and valuable approach. In the current landscape, there exists a repertoire of both novel and established metal-based catalysts (such as Pt, Pd, Rh, Ru, Co and Ni) that hold the potential to effectively convert greenhouse gases like CO_2 and CH_4 into syngas, utilizing both thermal and non-thermal processes [1, 2]. Among these catalysts, those based on low-cost active sites, particularly Ni, hold substantial promise. Notably, Ni demonstrates an interaction energy with CH_4 that is 25 times higher than that of Co [3, 4], rendering it a particularly attractive choice for catalytic applications in this context.

The active site Ni plays a crucial role in achieving effective dispersion and stabilization over appropriate support, particularly under the conditions of high-temperature DRM reactions. The choice of support material also significantly influences the catalytic performance of Ni. For instance, Ni supported on materials like titania, magnesia, alumina and zirconia exhibits a stronger interaction between the metal and the support, in comparison to Ni supported on silica, yttria, and ceria catalysts [5–7]. The formation of a metal support interface by NiO-MgO solid solution was frequently reported even at the lowest MgO loading [8]. Reduction of NiO-MgO under hydrogen surges small and stable Ni crystallites [9]. Further surface basicity and small dispersed Ni crystallites make NiO-MgO based catalyst a potential DRM catalyst with strong inhibition of carbon deposit [10]. Alumina-supported Ni catalyst has high thermal sustainability and great holding capacity of Ni [11, 12]. Zirconia-supported Ni catalyst has drawn the interest of the catalyst community due to the presence of dual acid–base sites, redox capability and maintaining high H_2/CO ratio (> 0.9) during DRM [13–15]. However, there are certain limitations associated with supported Ni catalysts. For instance, when Ni is supported on titania, the catalyst may encounter issues such as phase transitions in TiO_2 phases and reduced activity in DRM due to partial coverage of active Ni sites by titania [16]. Similarly, when Ni is supported on MgO, challenges

arise at higher calcination or pretreatment temperatures (> 700 °C) where the 5NiO-MgO solid solution becomes less reducible, resulting in larger Ni particle sizes and subsequent sintering [17, 18]. The activity of Ni catalysts supported on alumina could be hindered by factors such as limited diffusion of catalytically active Ni species within the alumina lattice, surface acidity and substantial coke deposition [19, 20]. Moreover, zirconia-supported Ni catalysts could face significant phase transitions of the zirconia phase at elevated DRM temperatures [21, 22].

At this point, two distinct approaches can be pursued. The first involves the addition of a small quantity of a second metal oxide (promoter) to the supported Ni catalyst, which significantly enhances its catalytic activity for DRM. However, this approach necessitates a precise synthetic strategy to achieve optimal loading, ensuring that the promoter does not obstruct the active catalytic sites. The second route involves utilizing a dual metal oxide support, thereby leveraging the strengths of each metal oxide to overcome any limitations inherent to the other. Among the options of titania, MgO, alumina and zirconia as supports, MgO stands out due to its cost-effectiveness.

In this context, we have prepared a support comprising 80wt% MgO combined with 20wt% of another metal oxide, chosen from among alumina, zirconia and titania. Each of these components possesses unique attributes; titania exhibits both rutile and anatase phases and is redox and acidic in nature, ZrO_2 displays both monoclinic and tetragonal phases and is redox and neutral, while Al_2O_3 is non-reducible but characterized by its acidic properties. The notable drawback of magnesia-supported Ni catalysts lies in their inferior reducibility and sintering susceptibility at elevated temperatures. Hence, investigating the role of a suitable metal oxide co-support that can compensate for MgO's limitations in the support becomes an intriguing path of exploration. Consequently, Ni dispersed over dual supports (MgO + TiO_2, MgO + Al_2O_3, MgO + ZrO_2) has been thoroughly examined for its performance in the DRM reaction. The investigation employs various characterization techniques, including X-ray diffraction (XRD), surface area and porosity analysis, RAMAN spectroscopy, transmission electron microscopy, temperature-programmed reduction/desorption/oxidation and thermogravimetric analysis. The thorough evaluation of the most synergistic metal oxide to complement MgO as a support for the Ni catalyst in DRM promises to deliver profound insights. The robust data correlations established herein are poised to significantly advance the development of a catalyst that holds the potential to be both economically viable and effective for large-scale DRM applications within the industrial domain.

2 Experimental

2.1 Material

Nickel nitrate hexahydrate [Ni $(NO_3)_2$.6H$_2$O, 98%, Alfa Aesar], γ-Al$_2$O$_3$ (Norton chemical process Product Corp, Ohio, USA), ZrO_2 (Daiichi Kigenso Kagaku Kogyo Co-LTD, Japan), TiO_2 (Aeoxide TiO$_2$ P25, Evonik Industries, Essen Germany) and SiO_2 (SoSal, Hamburg, Germany). MgO from BDH.

2.2 Catalyst Preparation

80wt% MgO + 20wt%MO$_x$ (M = Al, Zr, Ti) mixed oxide supports were prepared by mixing appropriate amounts of metal oxides and then after calcining for 5 h at 600 °C. 5wt% Ni loading was introduced by impregnating Ni $(NO_3)_2$·6H$_2$O solution over MgO + MO$_x$ (M = Al, Zr, Ti) support under stirring conditions. The prepared paste was dried at 120 °C for 20 h and then calcined for 5 h at 600 °C. The catalyst is abbreviated as 5Ni/MgO, 5Ni/MgO + Al$_2$O$_3$, 5Ni/MgO + TiO$_2$, 5Ni/MgO + ZrO$_2$.

2.3 Catalyst Characterization

Transmission electron microscopy (TEM), X-ray diffraction (XRD), Raman spectroscopy, H$_2$ temperature-programmed reduction (H$_2$-TPR), CO$_2$ temperature-programmed desorption (CO$_2$-TPD) and Thermogravimetric analysis (TGA) were used to characterize the catalysts. The Supporting Information (S1) provides a thorough explanation of the instruments and the characterization process.

2.4 Catalyst Activity Test

The dry reforming of the methane reaction was conducted in a stainless-steel fixed tube reactor (PID Eng. and Tech Micro Activity Reference, 9.1 mm internal diameter. and 30 cm length) over 0.1 g catalysts at 700 °C under 1 atm pressure. An axially positioned K-type (stainless sheathed) thermocouple monitors the catalyst bed temperature. Prior to the catalytic experiments, the catalyst is reduced at 600 °C for 60 min under H$_2$ (flow rate of 20 mL/min). The packed reactor was fed a mixture of gases in the proportions of 3:3:1 CH$_4$/CO$_2$/N$_2$, with a volume flow rate of 70 mL/min and an hourly gas velocity of 42,000 mL/ g$_{cat.}$ h. The product gas stream was examined using a GC (GC-2014 Shimadzu, columns: Porapak Q and Molecular

Sieve 5A) equipped with a thermal conductivity detector. H_2 yield percent and CO yield percent are calculated from the following formula.

$$H_2 \, \text{Yield} \, \% = \frac{\left(n_{H_2}\right)_{out}}{2 \times \left(n_{CH_4}\right)_{in}} \times 100$$

$$CO \, \text{Yield} \, \% = \frac{\left(n_{CO}\right)_{out}}{\left(n_{CH_4}\right)_{in} + \left(n_{CO_2}\right)_{in}} \times 100$$

where, $(n_{H_2})_{out}$ is Mole of H_2 in product (outlet), $(n_{CH_4})_{in}$ is mole of CH_4 in inlet, $(n_{CO})_{out}$ is mole of CO in product (outlet) and $(n_{CO})_{in}$ is mole of CO_2 in inlet.

3 Results and Discussion

3.1 Characterization Results and Discussion

N_2 adsorption isotherm, porosity distribution profiles and surface parameters of the 5Ni/MgO and 5Ni/MgO + MO_x (M = Al, Zr. Ti) catalysts are shown in Fig. 1. All catalysts exhibit a type IV isotherm with an H1 hysteresis loop, confirming the presence of mesopores [23] (Fig. 1a–d). Notably, the incorporation of 20wt% ZrO_2 to MgO results in a slightly lower surface area, pore olume and pore diameter for the 5Ni/MgO + ZrO_2 catalyst than 5Ni/MgO catalyst, whereas the incorporation of 20wt% TiO_2 along with MgO leads to a marginally higher surface area for the 5Ni/MgO + TiO_2 catalyst compared to the 5Ni/MgO catalyst (Fig. 1e). The use of 20wt% alumina combined with 80wt% magnesia as a support is particularly noteworthy. The 5Ni/MgO + Al_2O_3 catalyst demonstrates a surface area that is 1.5 times higher and a relatively greater pore volume than that of the 5Ni/ MgO catalyst. The rise in surface area after calcination in 5Ni/MgO + Al_2O_3 may be attributed to acid–base interaction of Al_2O_3-MgO, dispersion of acidic oxide Al_2O_3 over basic oxide MgO and loss of dangling hydroxyls [24, 25]. The distribution of pore sizes across the catalyst surface is depicted through the dV/dlogW versus W plot. Remarkably, the majority of pores observed in the 5Ni/MgO + Al_2O_3 catalyst have a size of 145 nm, which surpasses that of the other catalysts.

The X-ray diffraction patterns of Ni/MgO and Ni/ MgO + MO_x (M = Al, Zr. Ti) catalysts are presented in Fig. 2. The diffraction patterns for the magnesia-supported Ni catalyst and the 5Ni/MgO + Al_2O_3 catalyst are identical (Fig. 2a). The Ni/MgO catalyst exhibits diffraction peaks corresponding to the cubic $MgNiO_2$ phase (at Bragg's angle $2\theta = 36.8°$, 42.7°; JCPDS reference number: 00-024-0712) and cubic MgO phase (at $2\theta = 36.8°$, 42.7°, 62.1°, 74.5°, 78.43°; JCPDS reference number: 01-075-0447). In the

literature, cubic NiO peaks were reported at about 37.2° and 43.28°. In the case of the formation of NiO-MgO solid solution, the diffraction pattern about 43.28° is shifted to a lower angle (43.12°) [26]. Here, the diffraction pattern of the Ni/MgO catalyst is shifted to more lower angle (42.7°), indicating a proper mixing of cubic NiO and cubic MgO phase and the organization new cubic $MgNiO_2$ phase. Intriguingly, upon introducing 20wt% alumina along with 80% magnesia in support, the intensity of diffraction patterns decreases and shifts to a lower Braggs' angle. This shift indicates reduced crystallinity and an expansion of the cell parameter in the 5Ni/MgO + Al_2O_3 catalyst (Fig. 2b). Remarkably, the phases related to Al_2O_3 and $NiAl_2O_4$ that are typically observed in alumina-nickel-based catalyst systems are obviously absent. This phenomenon may be attributed to the diminished acid profile of alumina caused by basic MgO, which potentially hinders the formation of alumina-related phases [27]. Fahad et al. also found the loss of crystallinity upon dignifying the acid profile of alumina by basic lanthana [20]. Here also, the acid profile of alumina may also be diminished with basic MgO, which may retard the formation of alumina-related phases.

Furthermore, the addition of 20wt% titania alongside 80% magnesia leads to a further decrease in the crystallinity of the 5Ni/MgO + TiO_2 catalyst, coupled with a shift to a relatively higher Bragg's angle (Fig. 2e). This shift indicates partial contraction within the crystals. Previously, the calcination temperature above 500 °C was reported for the formation of $NiTiO_3$ phases over titanium and Ni-based material [28]. Here also, along with cubic $MgNiO_2$ phase and MgO phases, 5Ni/MgO + TiO_2 has additional peaks for rhombohedral $NiTiO_3$ phase (at Bragg's angle $2\theta = 24.1°$, 33°, 35.7°, 40.9°, 49.4°, 54.01°, 62.45°, 64.07°; JCPDS reference number: 00-033-0960). The 5Ni/MgO + TiO_2 catalyst is also populated by rutile TiO_2 phase (at $2\theta = 27.5°$, 36.1°, 41.3°, 54.4°, 56.7°, 69.1°; JCPDS reference number: 01-073-1765) and anatase TiO_2 phase (at $2\theta = 25.36°$, 37.9°, 48.1°, 54°, 55.2°; JCPDS reference number: 01-073-1764). Raman band of 5Ni/MgO + TiO_2 also confirms the presence of anatase TiO_2 phase (Raman band at 399 cm^{-1} (B_{1g}), 518 cm^{-1} (B_{1g}) and 639 cm^{-1} (E_g)) and rutile phase (Raman band at 447 cm^{-1} (E_g)) [29] (Fig. S3a). Interestingly, $NiTiO_3$ phase is observed in XRD but not in Raman results. It has been previously reported that the crystallization of $NiTiO_3$ initiates at 550–600 °C, while the ordering of the short-range $NiTiO_3$ structure begins at 650–700 °C [30, 31]. In our catalyst synthesis procedure, the calcination temperature is set at 600 °C. As a result, the rhombohedral $NiTiO_3$ phase is detectable through XRD but not through Raman spectroscopy. Upon the incorporation of 20wt% ZrO_2 along with 80% alumina support, the intensity of the diffraction peaks corresponding to the cubic $MgNiO_2$ phase and cubic MgO phases is minimized in the 5Ni/MgO + ZrO_2
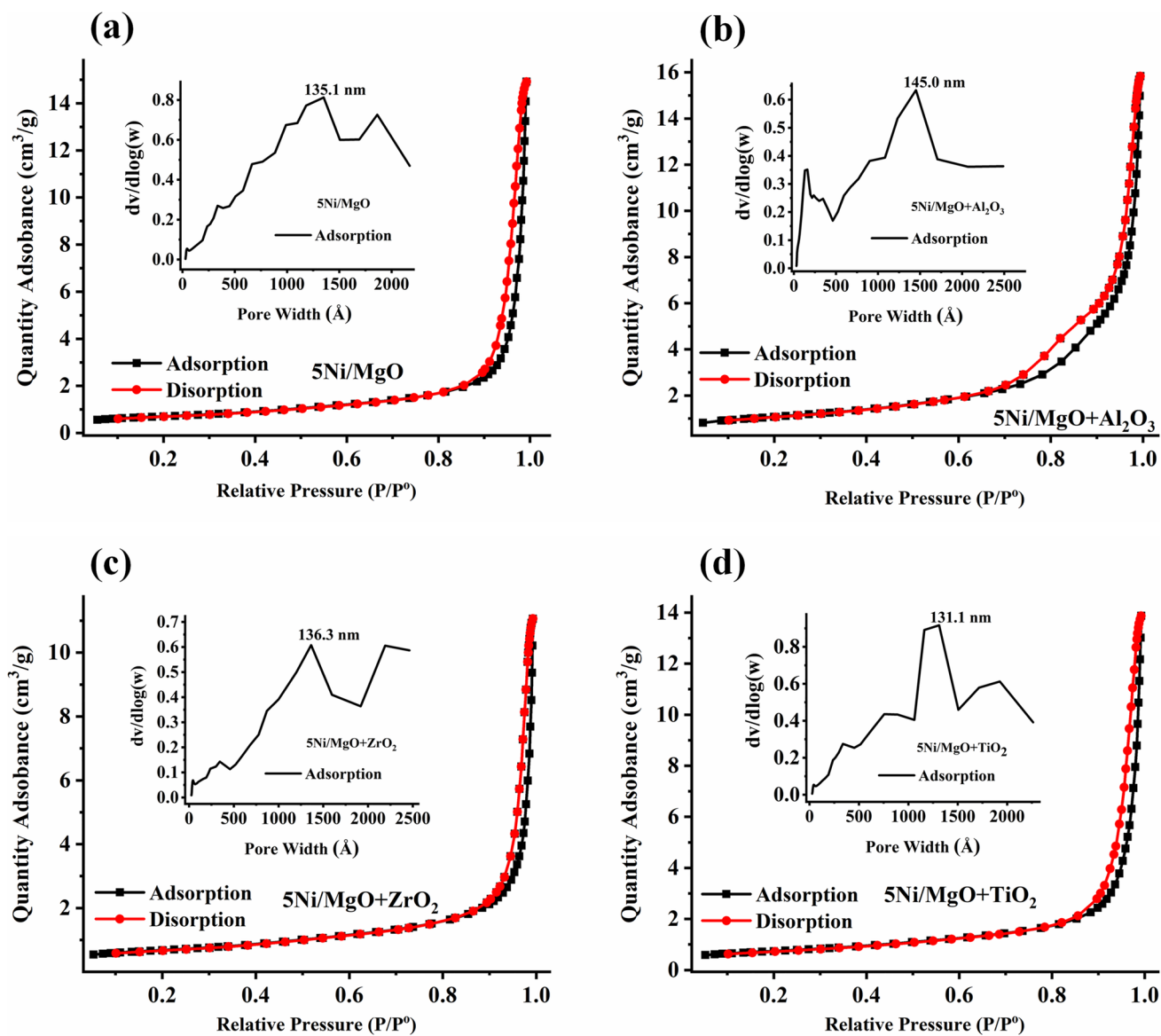
Catalyst Sample	Surface Area (m^2/g)	Pore Volume (cm^3/g)	Pore Diameter (nm)
5Ni/MgO	55.2	0.5	35.5
5Ni/MgO+Al$_2$O$_3$	84.9	0.6	21.2
5Ni/MgO+ZrO$_2$	52.9	0.4	31.2
5Ni/MgO+TiO$_2$	58.0	0.5	33.0

Fig. 1 **a–d** N$_2$ adsorption isotherm and porosity distribution profiles (inset) of 5Ni/MgO and 5Ni/MgO + MO$_x$ (M = Al, Zr. Ti) catalysts. **e** The surface area, pore volume and pore diameter of 5Ni/MgO and 5Ni/MgO + MO$_x$ (M = Al, Zr. Ti) catalysts
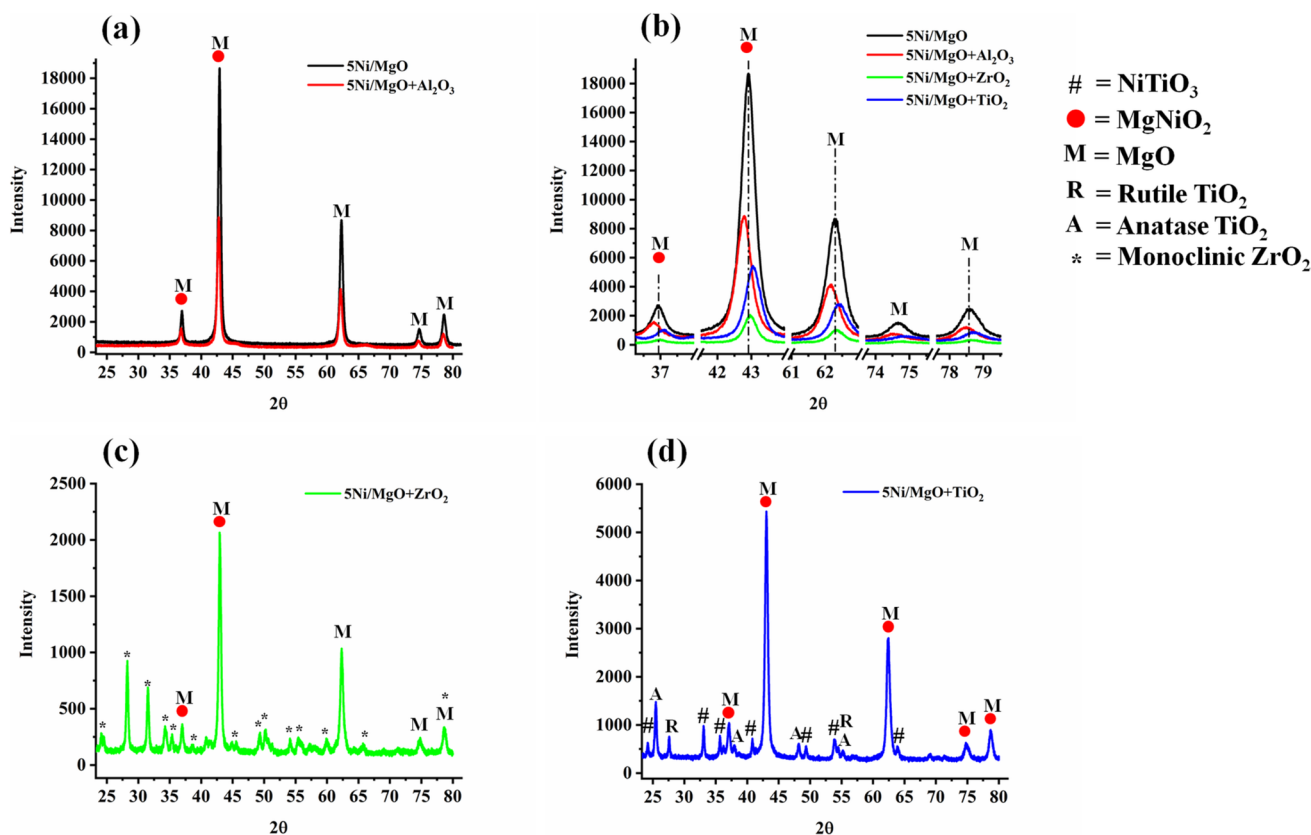
Fig. 2 X-ray diffraction profile of **a** 5Ni/MgO and 5Ni/MgO + Al$_2$O$_3$ catalyst, **b** 5Ni/MgO and 5Ni/MgO + MO$_x$ (M = Al, Zr. Ti) catalysts, **c** 5Ni/MgO + ZrO$_2$ catalyst, **d** 5Ni/MgO + TiO$_2$ catalyst

catalyst (Fig. 2c). Additionally, the 5Ni/MgO + ZrO$_2$ catalyst exhibits new diffraction peaks for monoclinic ZrO$_2$ (at 2θ = 24.1°, 28.2°, 31.5°, 34.2°, 35.3°, 49.3°, 50.2°; JCPDS reference number: 00-007-0343). The monoclinic zirconia phase is further validated by the presence of characteristic Raman bands at 179 cm^{-1}, 379 cm^{-1}, 476 cm^{-1}, 536 cm^{-1}, 559 cm^{-1}, 610 cm^{-1} and 636 cm^{-1} [32–34] (Fig. S3b).

The H$_2$-temperature programmed reduction profiles of 5Ni/MgO and 5Ni/MgO + MO$_x$ (M = Al, Zr, Ti) catalysts are shown in Fig. 3a. The MgO-supported Ni catalyst reducibility pattern can be broadly categorized into two regions. Firstly, a broad reduction peak is observed below 600 °C, attributed to reducible NiO interacting with support with moderate strength. Secondly, another broad peak is evident above 600 °C, corresponding to reducible NiO exhibiting a strong interaction with the support [35]. Previously, the peak of about 800 °C was reported for the reduction of Ni^{+2} located in the subsurface layer of MgO. It shows a very strong interaction between NiO and MgO [10]. XRD results show the presence of MgNiO$_2$ phase where Ni^{+2} is in very strong interaction with MgO. So, the peak in the higher temperature (~ 800 °C) can be attributed to the reduction of Ni^{+2} from the MgNiO$_2$ phase.

Remarkably, when the catalyst support includes 20wt% ZrO$_2$ and 80wt% MgO, the intensity of both reduction peaks is notably decreased in the 5Ni/MgO + ZrO$_2$ catalyst. Conversely, with the incorporation of 20wt% alumina alongside magnesia in the support, the intensity of the first reduction peak is diminished, while the second reduction peak is evidently intensified and broadened in the 5Ni/MgO + Al$_2$O$_3$ catalyst. This observation implies the prevalence of a higher concentration of "strongly interacted NiO species" over the 5Ni/MgO + Al$_2$O$_3$ catalyst compared to both the 5Ni/MgO + ZrO$_2$ and 5Ni/MgO catalysts. Additionally, the 5Ni/MgO + TiO$_2$ catalyst displays an additional distinct reduction peak at 655 °C, corresponding to the reduction of NiTiO$_3$ [28]. This observation is consistent with the detection of the NiTiO$_3$ phase in XRD analysis for the 5Ni/MgO + TiO$_2$ catalyst.

In this context, the catalyst is subjected to reduction prior to the DRM reaction, ensuring that the catalyst's surface exclusively presents active sites for CH$_4$ decomposition. Furthermore, the basicity of the reduced catalyst surface plays a pivotal role in its potential interaction with CO$_2$. Hence, after comprehending the reducibility profile of the catalyst, it becomes essential to delve into its basic profile subsequent to

reduction. To achieve this, a CO_2-temperature programmed desorption (CO_2-TPD) analysis of the reduced catalyst is conducted and depicted in Fig. 3b. The basic profile of the reduced catalyst is summarized into three distinct regions. Peaks appearing at around 150, 280 and 560 °C correspond to the interaction of CO_2 with weak basic sites (associated with surface hydroxyl groups) [36, 37], moderate-strength basic sites (involving surface oxygen anion) [35, 38] and strong basic sites, respectively [39, 40]. It is worth noting that the CO_2-TPD profile of the reduced 5Ni/MgO + Al$_2$O$_3$ catalyst exhibits a subtle shift towards relatively lower temperatures.

NiO undergoes a transformation upon reduction into metallic Ni, providing the active sites for the subsequent DRM reaction. During this process, CH_4 is decomposed into CH_x and H_2 over the metallic Ni sites, while CO_2 ideally oxidizes CH_x species. Over time, as the reaction progresses within the catalyst chamber, both oxidizing CO_2 gas and reducing H_2 gas (a product of the DRM reaction) are present. This dynamic interplay of CO_2 and H_2 can potentially lead to modifications in the concentration and strength of active sites, primarily the metallic Ni species. To gain deeper insights into the exact nature of the active sites under oxidizing and reducing gas environments, we have conducted cyclic sequential experiments involving hydrogen temperature-programmed reduction (H$_2$-TPR), CO_2 temperature-programmed desorption (CO_2-TPD) and another H$_2$-TPR step (Figs. 3c–e, S4). In this sequential experiment, the catalyst is initially reduced under H_2 (H$_2$-TPR), followed by an oxidative step under CO_2-TPD. Subsequently, the catalyst is subjected to another H_2 environment for potential re-reduction (H$_2$-TPR).

Through this sequential treatment involving reducing and oxidizing gases, a notable shift in the reducibility pattern of all catalysts towards the 200–300 °C range is observed. This shift indicates that the catalysts exhibit enhanced reducibility under the influence of the oxidizing/reducing gas mixture that is characteristic of the DRM reaction. This suggests that the active sites on the catalyst are readily accessible even at relatively lower temperatures under these oxidizing and reducing conditions. Furthermore, the intensity of this reduction peak follows the order: 5Ni/MgO + Al$_2$O$_3$ > 5Ni/MgO + TiO$_2$ > 5Ni/MgO + ZrO$_2$ > 5Ni/MgO (Fig. 3f). Remarkably, the reducibility pattern of 5Ni/MgO + Al$_2$O$_3$ under oxidizing and reducing gas environments stands out with a single intense reduction peak observed at 244 °C. This contrasts with the other catalysts, which exhibit split peaks at the same temperature. This unique pattern points to the presence of a specific type of active site on the 5Ni/MgO + Al$_2$O$_3$ catalyst under oxidizing and reducing gas conditions.

During the DRM reaction, the CH_x species oxidation delay can lead to carbon deposit accumulation on the catalyst surface. The extent of carbon deposition that can be oxidized by oxygen is reflected in the weight loss profiles of the spent catalysts under thermogravimetry analysis (Fig. 4a). Notably, the 5Ni/MgO + TiO$_2$ catalyst exhibits a substantial weight loss of approximately ~ 74%, indicating a significant presence of active carbon or oxidizable carbon deposits. In contrast, the remaining catalysts show weight losses ranging from 11 to 13%, suggesting lower levels of carbon deposits. It is worth noting that the 5Ni/MgO + TiO$_2$ catalyst might also contain inert carbon species that remain unoxidized during the TGA analysis.

To delve deeper into the characteristics of the carbon deposits, Raman spectra of the spent catalysts were recorded (Fig. 4b). In Raman spectra, the wavenumbers at $1340 + 5$ cm^{-1} and $1570 + 10$ cm^{-1} correspond to the disordered/amorphous/defective carbon (D band) and well-ordered/graphitic carbon (G band), respectively [41]. Additionally, the 2D band is observed at 2673 cm^{-1} [42]. All these three bands are evident in the case of the spent 5Ni/MgO catalyst. Upon incorporating 20wt% titania with 80wt% MgO in support, the spent-5Ni/MgO + TiO$_2$ catalyst exhibits notably higher intensities for these bands. This indicates that the spent-5Ni/MgO + TiO$_2$ catalyst has the highest amount of disordered/defective and ordered/graphitic carbon deposits.

Upon incorporating 20wt% ZrO$_2$ along with 80wt% MgO in support, the Raman peak intensity decreases compared to the spent 5Ni/MgO + TiO$_2$. Notably, a new peak around 2218 cm^{-1} emerges in the Raman spectrum of the spent 5Ni/MgO + ZrO$_2$ catalyst. In literature, the stretching mode of sp^3-carbon (without hydrogen) has been reported at ~ 2200 cm^{-1} [43]. A more diverse array of carbon deposits is observed when Ni is supported over a catalyst comprising 20wt% alumina and 80wt% magnesia. The Raman band intensity associated with the peak mentioned above is lower for the spent 5Ni/MgO + Al$_2$O$_3$ than the spent 5Ni/MgO + ZrO$_2$ catalyst. Intriguingly, two new Raman bands, at approximately 1690 cm^{-1} and 2092 cm^{-1}, are also observed over the spent 5Ni/MgO + Al$_2$O$_3$ catalyst. Raman bands within the 1690–2150 cm^{-1} range are associated with the presence of non-suspended commensurate, incommensurate (folded) and suspended graphene layers [44].

The Energy Dispersive X-ray (EDX) spectra of 5Ni/MgO and 5Ni/MgO + MO$_x$ (M = Al, Zr. Ti) catalysts are shown in Fig. S5. Upon using dual metal oxide supports, the surface enrichment of Ni atoms are recognized over 5Ni/MgO + MO$_x$ (M = Al, Zr. Ti) catalyst than 5Ni/MgO catalyst. Out of all the catalysts, the 5Ni/MgO + Al$_2$O$_3$ catalyst has the highest Ni enrichment on its surface. The TEM image of both the fresh 5Ni/MgO + Al$_2$O$_3$ and spent catalyst are shown in Fig. 5. Notably, the average particle size has increased to 4 nm in the spent 5Ni/MgO + Al$_2$O$_3$,
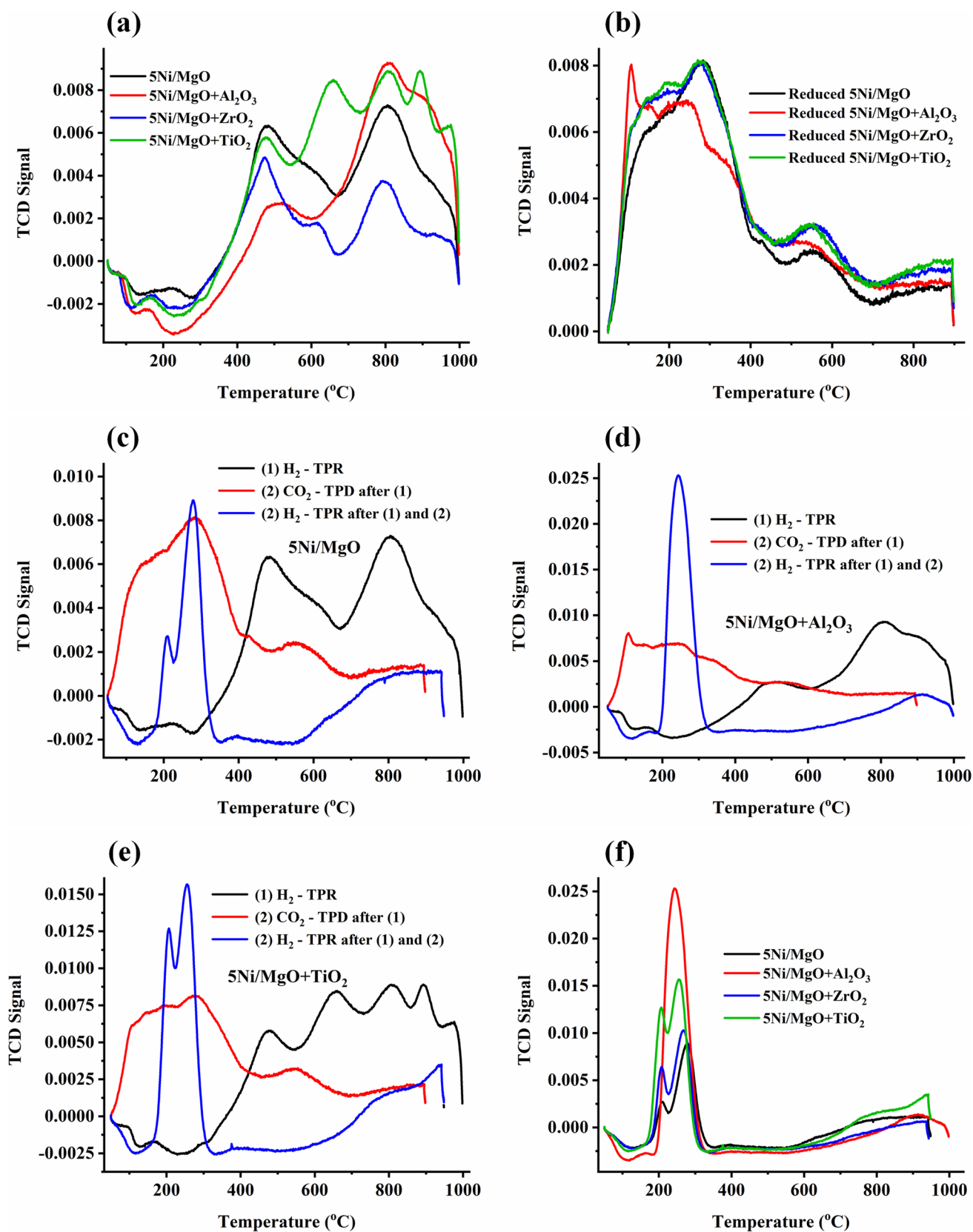
◀**Fig. 3 a** H$_2$-temperature programmed reduction of 5Ni/MgO and 5Ni/MgO + MO$_x$ (M = Al, Zr. Ti) catalysts. **b** CO$_2$-temperature programmed desorption of reduced-5Ni/MgO and reduced-5Ni/MgO + MO$_x$ (M = Al, Zr. Ti) catalysts. **c** cyclic H$_2$TPR-CO$_2$TPD-H$_2$TPR profile of 5Ni/MgO. **d** cyclic H$_2$TPR-CO$_2$TPD-H$_2$TPR profile of 5Ni/MgO + Al$_2$O$_3$. **e** cyclic H$_2$TPR-CO$_2$TPD-H$_2$TPR profile of 5Ni/MgO + TiO$_2$. **f** reducibility profile after sequential treatment with oxidizing and reducing gas of 5Ni/MgO and 5Ni/MgO + MO$_x$ (M = Al, Zr. Ti) catalysts

compared to the initial size of 3.7 nm observed in the fresh 5Ni/MgO + Al$_2$O$_3$ catalyst.

3.2 Activity Results and Discussion

The presence of the cubic MgNiO$_2$ phase is a common feature observed in both the "MgO-supported Ni" and "MgO + MO$_x$ (M = Ti, Al, Zr)-supported Ni" catalysts. The catalyst's metallic Ni components serve as active sites for the decomposition of CH$_4$ and these sites are generated by reducing the catalysts using H$_2$. After reduction, the catalysts exhibit a range of basic sites, varying in strength from weak to strong, which are involved in interacting with CO$_2$. The interplay between CH$_4$ decomposition and CO$_2$ interaction is pivotal in driving the syngas formation pathway.

However, despite these factors, the complexity of the reaction mechanism cannot be fully captured by these conditions alone. This is due to the inherent nature of CO$_2$, which acts as an oxidizing gas and H$_2$, a reducing gas. The presence of these gases in the system can dynamically influence both the population and accessibility of the active sites. The cyclic H$_2$TPR-CO$_2$TPD-H$_2$TPR experiment offers valuable insights into this aspect, revealing an enhancement in the higher threshold of reducibility for both the "MgO-supported Ni" and "MgO + MO$_x$ (M = Ti, Al, Zr)-supported Ni" catalyst systems under conditions of both oxidizing and reducing environments during DRM. In essence, as the reaction progresses, the catalysts move back and forth between oxidizing (CO$_2$) and reducing (H$_2$) gas environments. This dynamic equilibrium results in the accessible active sites of "metallic Ni" being made available at considerably lower temperatures, thereby significantly contributing to the effectiveness of the DRM process.

The catalytic activity results for the 5Ni/MgO and 5Ni/MgO + MO$_x$ (M = Al, Zr. Ti) catalysts are shown in Fig. 6. The MgO-supported Ni catalyst exhibits a surface area of 55.2 m^2/g along with reducible NiO, derived from the cubic MgNiO$_2$ phase, which interacts with surface from moderate to strong strength. This phenomenon of Ni interaction with MgO support has been previously elucidated by Zou et al. through density functional theory and kinetic Monte Carlo simulations [45]. Furthermore, the reduced 5Ni/MgO catalyst is characterized by an array of basic sites spanning from weak to strong strengths, poised for potential interaction

with CO$_2$. The reduced catalyst provides access to metallic Ni sites that facilitate the CH$_4$ decomposition process, along with offering basic sites for the interaction of CO$_2$, thereby initiating the dry reforming of methane reaction. Moreover, the shifting balance between oxidizing and reducing environments during the DRM reaction expedites the accessibility of metallic Ni sites at lower temperatures. This synergy culminates in the 5Ni/MgO catalyst, displaying a consistent H$_2$ yield of 70–69% (CO yield of 73–72%) over a duration of 430 min in the time on stream test. Notably, the spent 5Ni/MgO catalyst demonstrates minimal weight loss and a low accumulation of graphitic carbon. The relatively higher CO yield compared to the H$_2$ yield implies the possible occurrence of side reactions, such as the reverse water gas shift reaction, alongside the primary dry reforming of methane reaction.

Incorporating 20wt% ZrO$_2$ alongside 80% MgO in the catalyst of 5Ni/MgO + ZrO$_2$ results in a reduction of surface area compared to the 5Ni/MgO catalyst. Additionally, the catalyst exhibits the least crystallinity and a monoclinic phase, a characteristic associated with potential phase transition and catalyst instability [21]. The fresh 5Ni/MgO + ZrO$_2$ catalyst demonstrates inferior reducibility compared to the 5Ni/MgO catalyst. Notably, the reducibility pattern of 5Ni/MgO + ZrO$_2$ does not significantly differ from that of the 5Ni/MgO catalyst under oxidizing and reducing environments during the DRM reaction.

The weight loss profile of the spent 5Ni/MgO + ZrO$_2$ catalyst is akin to that of the spent 5Ni/MgO catalyst, albeit with a relatively higher content of graphitic carbon. The spent catalyst also reveals an additional deposit of sp^3-carbon (without hydrogen). The overall impact on the catalytic performance is evident in the H$_2$ yield of the 5Ni/MgO + ZrO$_2$ catalyst, which is only 54% and further decreases to 46% during the 430 min time on stream. The CO yield, similarly, remained between 62 and 56% throughout the 430 min time on stream.

The 5Ni/MgO + TiO$_2$ catalyst exhibits a notably higher surface area compared to the 5Ni/MgO catalyst. This catalyst also features a partially contracted lattice and lower crystallinity in comparison. Additionally, it includes reducible rhombohedral NiTiO$_3$ phases alongside the cubic MgNiO$_2$ phase. Consequently, the 5Ni/MgO + TiO$_2$ catalyst boasts the highest population of catalytically active Ni species (derived from the reduction of both MgNiO$_2$ and NiTiO$_3$) among the various catalyst systems considered for DRM. Moreover, under oxidizing and reducing conditions during the DRM process, the 5Ni/MgO + TiO$_2$ catalyst showcases an enhanced degree of reducibility compared to the 5Ni/MgO + ZrO$_2$ and 5Ni/MgO catalysts.

Turning to the spent catalyst analysis, the TGA and Raman profiles of the spent 5Ni/MgO + TiO$_2$ catalyst reveal a substantial weight loss (73.9%) and the highest
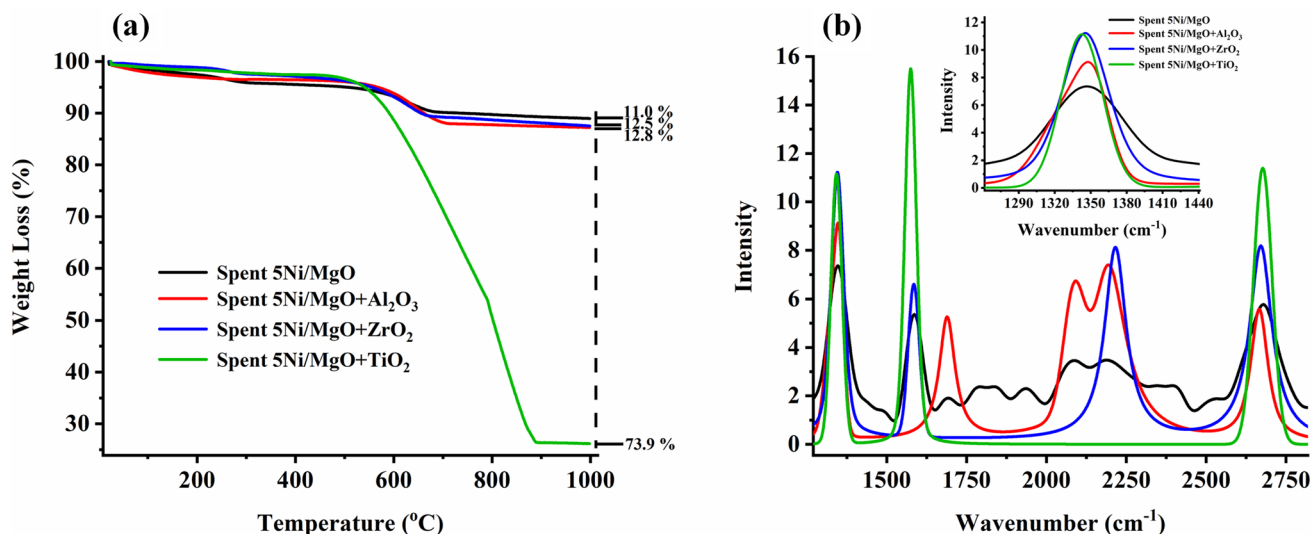
Fig. 4 **a** Thermogravimetry analysis of spent-5Ni/MgO and spent-5Ni/MgO+MO$_x$ (M = Al, Zr. Ti) catalysts. **b** Raman spectra of spent-5Ni/MgO and spent-5Ni/MgO+MO$_x$ (M = Al, Zr. Ti) catalysts
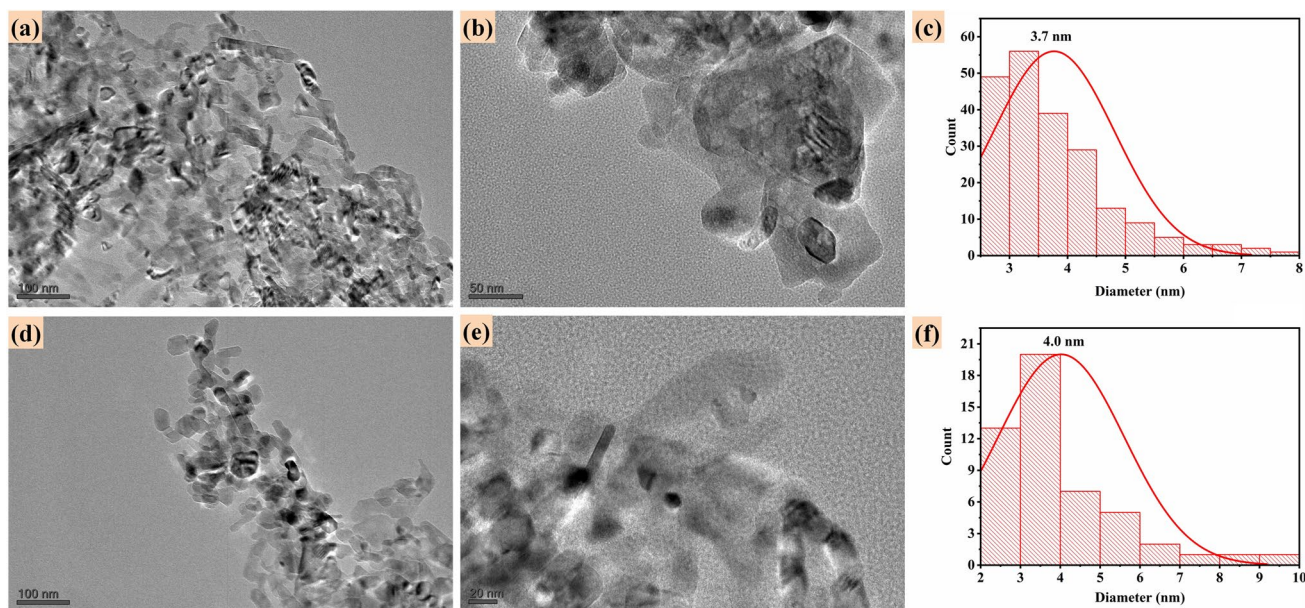

Fig. 5 **a** TEM image of 5Ni/MgO+Al$_2$O$_3$ at 100 nm scale. **b** TEM image of 5Ni/MgO+Al$_2$O$_3$ at 50 nm scale. **c** Particle size distribution of Ni over 5Ni/MgO+Al$_2$O$_3$. **d** TEM image of spent 5Ni/MgO+Al$_2$O$_3$ at 100 nm scale. **e** TEM image of spent-5Ni/MgO+Al$_2$O$_3$ at 50 nm scale. **f** Particle size distribution of Ni over spent-5Ni/MgO+Al$_2$O$_3$

accumulation of "graphitic and defective" carbon deposits on the catalyst surface. Despite presenting a greater number of active sites, the catalytic performance of the 5Ni/MgO+TiO$_2$ catalyst is hindered by severe carbon deposition, leading to diminished activity compared to the 5Ni/MgO catalyst. Throughout the 430 min time on stream, the 5Ni/MgO+TiO$_2$ catalyst achieves H$_2$ yields of 63–60% and CO yields of 70–65%.

The incorporation of 20wt% Al$_2$O$_3$ along with 80wt%MgO brings about significant modifications in the physio-chemical surface composition of the 5Ni/MgO+Al$_2$O$_3$ catalyst. Notably, the catalyst's crystallinity decreases compared to the 5Ni/MgO catalyst, while the lattice is relatively expanded, and the surface area extends to 1.5 times that of 5Ni/MgO. The fresh 5Ni/MgO+Al$_2$O$_3$ catalyst surface exhibits the highest concentration of "strongly
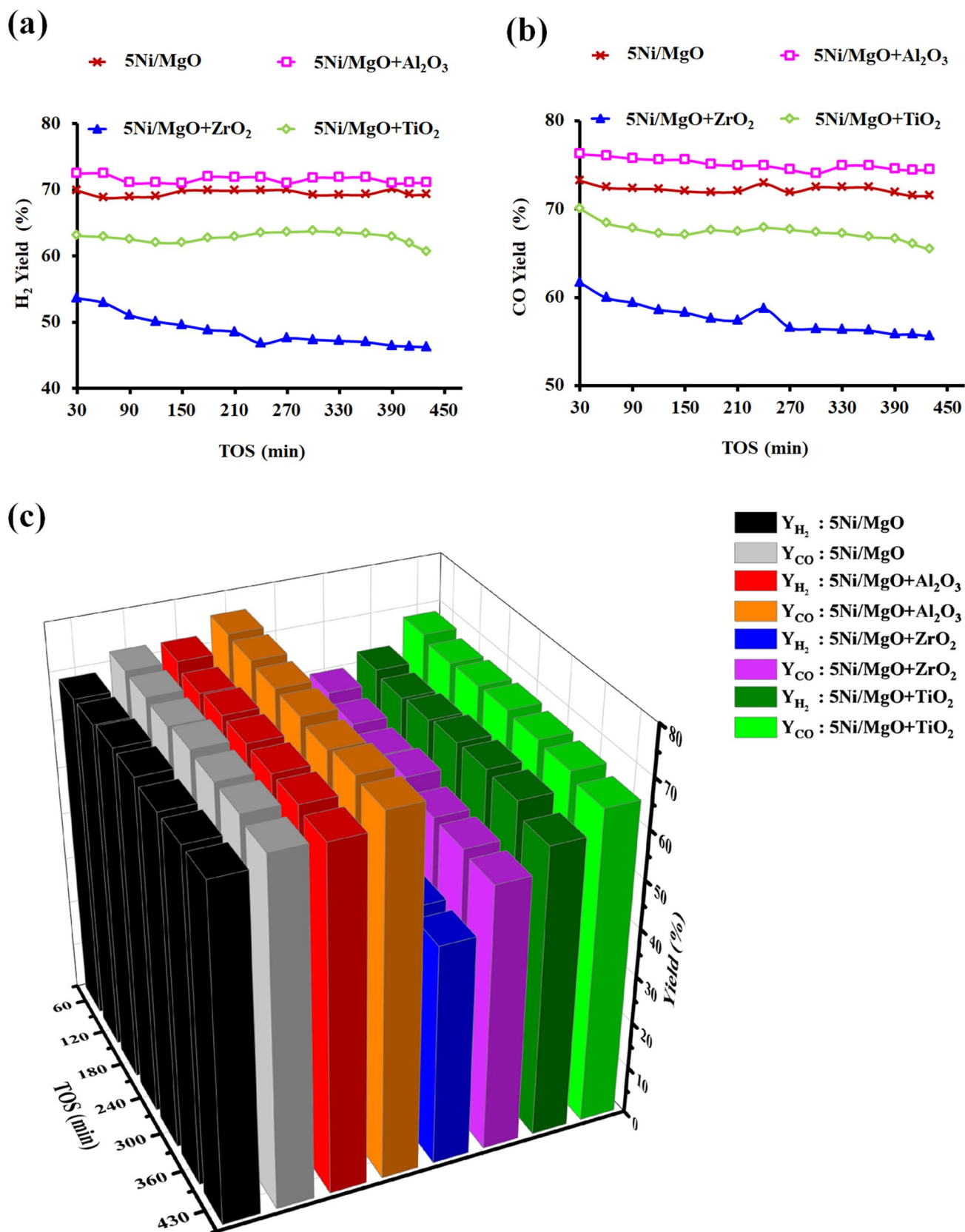
Fig. 6 Catalytic activity results over 5Ni/MgO and 5Ni/MgO + MO$_x$ (M = Al, Zr. Ti) catalysts, **a** H$_2$-yield (%) vs time on stream (TOS), **b** CO-yield (%) vs time on stream (TOS), **c** "H$_2$ yield(%) and CO yield (%)" vs time on stream (TOS)

Table 1 Comparative catalyst activity for dry reforming of methane over closely related catalyst systems

SI No	Catalyst name	MP	ID (mm)	%wt of Ni	CW (mg)	Feed ratio			GHSV L/(g$_{cat}$h)	TOS (h)	Tem (°C)	Y_{H_2} (%)	References
						CH$_4$	CO$_2$	CG (N$_2$)					
1	Ni/Al$_2$O$_3$	SG	–	15	200	1	1	0	24	8	800	63	[46]
2	Ni/Al$_2$O$_3$	UI	–	10.1	–	1	1	0	70	70	600	22	[47]
3	Ni/Al$_2$O$_3$	I	9.4	3.8	600	17	17	2	3.6	5.3	700	70	[48]
4	Ni/Al	I-CI	–	10	50	1	1	3	60	5	550	12	[49]
5	Ni/Al$_2$O$_3$	I	5	10	–	1	1	–	24	24	550	10	[50]
6	Ni/Al$_2$O$_3$	I	5	10	–	1	1	–	24	24	750	61	[50]
7	Ni/Al$_2$O$_3$	I	5	10	–	1	1	–	24	24	650	30	[50]
8	5Ni/Zr	I	9.1	5	100	3	3	1	42	7	700	43	[51]
9	Ni/Zr	I	–	7.65	150	55	35	10	40	0.75	800	29	[52]
10	Ni/Zr	I	–	7.65	150	55	35	10	80	50	800	16	[52]
11	Ni/Zr	I	–	7.65	150	55	35	10	120	10	800	10	[52]
12	10Ni/ZrO$_2$-PP	I	–	10	50	1	1	2*	60	0.5	700	60	[53]
13	10Ni/ZrO$_2$-PC	I	–	10	50	1	1	2*	60	0.5	700	45	[53]
14	5Ni-SP-OA	I	6	5	100	1	1	0	24	6	700	45	[54]
15	Ni-SP-Imp	I	6	5	100	1	1	0	24	6	700	32	[54]
16	Ni-20/MSN	I	4	5	100	4	4	52	36	3	600	62	[55]
17	Ni-20/MSN	I	4	5	100	4	4	52	36	3	700	71	[55]
18	NiY/Al	I-CI	–	10	50	1	1	3	60	5	550	11	[49]
19	5Ni3TiAl	I	9	5	100	3	3	1	12	7	700	30	[56]
20	5Ni3MoAl	I	9	5	100	3	3	1	12	7	700	39	[56]
21	5Ni3SiAl	I	9	5	100	3	3	1	12	7	700	62	[56]
22	5Ni3WAl	I	9	5	100	3	3	1	12	7	700	62	[56]
23	Ni/LaZr	I	9.1	5	100	3	3	1	42	8	700	58	[57]
24	Ni/LaZr	I	–	7.58	75	55	35	10	120	10	800	11	[52]
25	Ni/LaZr	I	–	7.58	75	55	35	10	40	0.75	800	42	[52]
26	Ni/LaZr	I	–	7.58	75	55	35	10	80	50	800	24	[52]
27	Ni/CeZr	I	–	7.96	50	55	35	10	80	50	800	27	[52]
28	Ni/CeZr	I	–	7.96	50	55	35	10	120	10	800	13	[52]
29	5Ni/CeO$_2$-ZrO$_2$	SA	6.3	5	150	2	2	1	40	8	700	57	[58]
30	Ni/CeZr	I	–	7.96	50	55	35	10	40	0.75	800	48	[52]
31	5Ni-15Y-ZrO$_2$	I	–	5	100	3	3	1	42	7	700	64	[22]
32	5Ni/YZr	I	9.1	5	100	3	3	1	42	7	700	67	[59]
33	5Ni15YZr	I	9.1	5	100	3	3	1	42	7	700	55	[60]
34	5Ni5MgZr	I	9.1	5	100	3	3	1	42	7	700	23	[60]

Table 1 (continued)

SI No	Catalyst name	MP	ID (mm)	%wt of Ni	CW (mg)	Feed ratio			GHSV L/(g$_{cat}$.h)	TOS (h)	Tem (°C)	Y_{H_2} (%)	References
						CH$_4$	CO$_2$	CG (N$_2$)					
35	5Ni/MgO	I	9.1	5	100	3	3	1	42	7	700	69	This study
36	5Ni/MgO + Al$_2$O$_3$	I	9.1	5	100	3	3	1	42	7	700	71	
37	5Ni/MgO + ZrO$_2$	I	9.1	5	100	3	3	1	42	7	700	46	
38	5Ni/MgO + TiO$_2$	I	9.1	5	100	3	3	1	42	7	700	61	

CW catalyst weight, *MP* method of catalyst preparation, *ID* initial diameter, *CG* carrier gas (N$_2$), *I* impregnation, *SG* sol–gel, *UI* ultrasonication assisted impregnation, *PP* prepared by plasma heating, *PC* prepared by calcination, *SP* Mesoporous SiO$_2$ (316 m^2/g, pore diameter = 11.81 nm), *OA* oleic acid assisted, *MSN* mesoporous silica new, *I-CI* impregnation and then co-impregnation, *SA* surfactant-assisted method

*The symbol denotes argon as a carrier gas

interacted reducible-NiO species". EDX profile showed the highest Ni enrichment on the surface of 5Ni/MgO + Al$_2$O$_3$ catalyst than rest catalysts. Basic sites for CO$_2$ interaction are also accessible at slightly lower temperatures. These surface features contribute to achieving H$_2$ yields of up to 72.5% (with CO yields of up to 76%). Over time, under oxidizing and reducing conditions during DRM, the active sites become accessible at lower temperatures, with the highest accessibility observed over the 5Ni/MgO + Al$_2$O$_3$ catalyst. The spent 5Ni/MgO + Al$_2$O$_3$ catalyst experiences a weight loss of about 12.8%, similar to the spent 5Ni/MgO + ZrO$_2$ catalyst. The type of carbon deposit observed includes graphene layers and sp^3-carbon (without hydrogen) but no graphitic carbon. Overall, the catalytic activity remains stable, with H$_2$ yields not dropping below 71% (with CO yields of 74%) during the 430-min time on stream. The catalytic activity of the 5Ni/MgO + Al$_2$O$_3$ catalyst is optimal among the considered catalyst systems.

Comparing the catalytic activity of "metal oxide supported Ni" and "dual metal oxide supported Ni" catalysts for DRM (in terms of H$_2$ yield), as shown in Table 1 [22, 46–60], it is evident that the H$_2$ yield achieved by the 5Ni/MgO + Al$_2$O$_3$ catalyst is comparable to that of alumina-supported Ni catalyst [48] and MSN (mesoporous silica new) supported 20wt% Ni catalyst [55]. Notably, the former study employed six times more catalyst for the reaction, and the latter study used four times more Ni loading than the current catalyst in this study.

4 Conclusion

The study investigated promotor-free, MgO or MgO + MO$_x$ (M = Zr, Ti, Al) supported Ni-based catalyst system for the dry reforming of methane (DRM) to syngas. The reduced MgO-supported Ni catalyst exhibited good reducibility, a wide range of basic sites for CO$_2$ interaction, and active Ni sites derived from cubic MgNiO$_2$. The cyclic H$_2$TPR-CO$_2$TPD-H$_2$TPR experiment highlighted the increased accessibility of active Ni sites under both oxidizing and reducing environments during DRM, leading to a consistent ~70% H$_2$ yield over 430 min.

However, the addition of 20wt% ZrO$_2$ led to an unstable catalyst phase, reduced reducibility, and increased graphitic carbon deposition. This resulted in a significantly decreased H$_2$ yield of 46% over the same reaction time. On the other hand, the 5Ni/MgO + TiO$_2$ catalyst showed increased active Ni concentration due to the presence of rhombohedral NiTiO$_3$ along with MgNiO$_2$. It also exhibited enhanced reducibility under both oxidizing and reducing conditions, but extensive coke deposition limited its H$_2$ yield to 60%.

The addition of 20wt% Al$_2$O$_3$ with MgO support significantly modified the physio-chemical surface composition of

the catalyst. The 5Ni/MgO + Al$_2$O$_3$ catalyst demonstrated expanded lattice and surface area, a high concentration of "strongly interacted reducible NiO species", and the highest accessible active sites during DRM. Interestingly, the spent-5Ni/MgO + Al$_2$O$_3$ catalyst did not show a graphitic carbon peak but a carbon peak for graphene layers and sp^3-C (without hydrogen). This catalyst maintained a constant H$_2$ yield of 71% (CO yield of 74%) over the 430 min reaction time, making it a promising candidate for DRM applications.

Overall, the study provides valuable insights into the effects of promotor-free Ni-based different catalyst supports and compositions on DRM performance, highlighting the role of reducibility, basicity and coke deposition in achieving sustainable and efficient syngas production.

Declarations

Ethical Approval The views and opinions expressed in this paper do not necessarily reflect those of the European Commission or the Special EU Programmes Body (SEUPB).

References

1. Al-Fatesh AS, Patel N, Fakeeha AH et al (2023) Reforming of methane: effects of active metals, supports, and promoters. Catal Rev. https://doi.org/10.1080/01614940.2023.2211447

2. Chen H, Mu Y, Xu S et al (2020) Recent advances in non-thermal plasma (NTP) catalysis towards C1 chemistry. Chin J Chem Eng 28:2010–2021. https://doi.org/10.1016/j.cjche.2020.05.027

3. Gallego GS, Batiot-Dupeyrat C, Barrault J et al (2008) Dry reforming of methane over LaNi1-yByO3±δ (B=Mg, Co) perovskites used as catalyst precursor. Appl Catal A Gen 334:251–258. https://doi.org/10.1016/j.apcata.2007.10.010

4. Liao MS, Au CT, Ng CF (1997) Methane dissociation on Ni, Pd, Pt and Cu metal (111) surfaces—a theoretical comparative study. Chem Phys Lett 272:445–452. https://doi.org/10.1016/s0009-2614(97)00555-1

5. Xu Y, Du XH, Li J et al (2019) A comparison of Al$_2$O$_3$ and SiO$_2$ supported Ni-based catalysts in their performance for the dry reforming of methane. J Fuel Chem Technol 47:199–208. https://doi.org/10.1016/s1872-5813(19)30010-6

6. Al-Fatesh AS (2017) Promotional effect of Gd over Ni/Y$_2$O$_3$ catalyst used in dry reforming of CH4 for H$_2$ production. Int J Hydrogen Energy 42:18805–18816. https://doi.org/10.1016/j.ijhydene.2017.06.165

7. Araiza DG, Arcos DG, Gómez-Cortés A, Díaz G (2021) Dry reforming of methane over Pt-Ni/CeO$_2$ catalysts: effect of the metal composition on the stability. Catal Today 360:46–54. https://doi.org/10.1016/j.cattod.2019.06.018

8. García V, Fernández JJ, Ruíz W et al (2009) Effect of MgO addition on the basicity of Ni/ZrO$_2$ and on its catalytic activity in carbon dioxide reforming of methane. Catal Commun 11:240–246. https://doi.org/10.1016/j.catcom.2009.10.003

9. Kuzmin A, Mironova N (1998) Composition dependence of the lattice parameter in solid solutions. J Phys Condens Matter 10:7937. https://doi.org/10.1088/0953-8984/10/36/004

10. Zanganeh R, Rezaei M, Zamaniyan A (2013) Dry reforming of methane to synthesis gas on NiO–MgO nanocrystalline solid solution catalysts. Int J Hydrogen Energy 38:3012–3018. https://doi.org/10.1016/j.ijhydene.2012.12.089

11. Zhou L, Li L, Wei N et al (2015) Effect of NiAl$_2$O$_4$ formation on Ni/Al$_2$O$_3$ stability during dry reforming of methane. ChemCatChem 7:2508–2516. https://doi.org/10.1002/cctc.201500379

12. Sepehri S, Rezaei M, Garbarino G, Busca G (2016) Preparation and characterization of mesoporous nanocrystalline La-, Ce-, Zr-, Sr-containing NiAl$_2$O$_3$ methane autothermal reforming catalysts. Int J Hydrogen Energy 41:8855–8862. https://doi.org/10.1016/j.ijhydene.2016.03.139

13. Barroso-Quiroga MM, Castro-Luna AE (2010) Catalytic activity and effect of modifiers on Ni-based catalysts for the dry reforming of methane. Int J Hydrogen Energy 35:6052–6056. https://doi.org/10.1016/j.ijhydene.2009.12.073

14. Rezaei M, Alavi SM, Sahebdelfar S, Yan ZF (2007) Mesoporous nanocrystalline zirconia powders: a promising support for nickel catalyst in CH4 reforming with CO$_2$. Mater Lett 61:2628–2631. https://doi.org/10.1016/j.matlet.2006.10.053

15. Rezaei M, Alavi SM, Sahebdelfar S, Yan Z-F (2008) Effects of K$_2$O promoter on the activity and stability of nickel catalysts supported on mesoporous nanocrystalline zirconia in CH4 reforming with CO$_2$. Energy Fuels 22:2195–2202. https://doi.org/10.1021/ef800114e

16. Shah M, Bordoloi A, Nayak AK, Mondal P (2019) Effect of Ti/Al ratio on the performance of Ni/TiO$_2$-Al$_2$O$_3$ catalyst for methane reforming with CO$_2$. Fuel Process Technol 192:21–35. https://doi.org/10.1016/j.fuproc.2019.04.010

17. Usman M, Wan Daud WMA (2016) An investigation on the influence of catalyst composition, calcination and reduction temperatures on Ni/MgO catalyst for dry reforming of methane. RSC Adv 6:91603–91616. https://doi.org/10.1039/c6ra15256b

18. Jafarbegloo M, Tarlani A, Mesbah AW et al (2016) NiO-MgO solid solution prepared by sol-gel method as precursor for Ni/MgO methane dry reforming catalyst: effect of calcination

temperature on catalytic performance. Catal Lett 146:238–248. https://doi.org/10.1007/s10562-015-1638-9

19. Cai M, Wen J, Chu W et al (2011) Methanation of carbon dioxide on Ni/ZrO$_2$-Al$_2$O$_3$ catalysts: effects of ZrO$_2$ promoter and preparation method of novel ZrO$_2$-Al2O$_3$ carrier. J Nat Gas Chem 20:318–324. https://doi.org/10.1016/S1003-9953(10)60187-9

20. Al-mubaddel FS, Kumar R, Lanre M et al (2021) ScienceDirect optimizing acido-basic profile of support in Ni supported La$_2$O$_3$ÞAl$_2$O$_3$ catalyst for dry reforming of methane. Int J Hydrogen Energy 46:14225–14235. https://doi.org/10.1016/j.ijhydene.2021.01.173

21. Majumdar D, Chatterjee D (1991) X-ray photoelectron spectroscopic studies on yttria, zirconia, and yttria-stabilized zirconia. J Appl Phys 70:988–992. https://doi.org/10.1063/1.349611

22. Patel R, Fakeeha AH, Kasim SO et al (2021) Optimizing yttria-zirconia proportions in Ni supported catalyst system for H$_2$ production through dry reforming of methane. Mol Catal 510:111676. https://doi.org/10.1016/j.mcat.2021.111676

23. Kumar R (2022) Surface characterization techniques. De Gruyter, Berlin

24. Jiang D, Zhao B, Xie Y et al (2001) Structure and basicity of γ-Al$_2$O$_3$-supported MgO and its application to mercaptan oxidation. Appl Catal A Gen 219:69–78. https://doi.org/10.1016/S0926-860X(01)00660-3

25. Jackson DHK, O'Neill BJ, Lee J et al (2015) Tuning acid-base properties using Mg–Al oxide atomic layer deposition. ACS Appl Mater Interfaces 7:16573–16580. https://doi.org/10.1021/acsami.5b04107

26. Al-Fatesh AS, Kumar R, Fakeeha AH et al (2020) Promotional effect of magnesium oxide for a stable nickel-based catalyst in dry reforming of methane. Sci Rep 10:13861. https://doi.org/10.1038/s41598-020-70930-1

27. Nortier P, Fourre P, Saad ABM et al (1990) Effects of crystallinity and morphology on the surface properties ofalumina. Appl Catal 61:141–160. https://doi.org/10.1016/S0166-9834(00)82140-5

28. de Bokx PK, Bonne RLC, Geus JW (1987) Strong metal-support interaction in Ni/TiO2 catalysts: the origin of TiOx moieties on the surface of nickel particles. Appl Catal 30:33–46. https://doi.org/10.1016/S0166-9834(00)81009-X

29. Chen CA, Huang YS, Chung WH et al (2009) Raman spectroscopy study of the phase transformation on nanocrystalline titania films prepared via metal organic vapour deposition. J Mater Sci Mater Electron 20:303–306. https://doi.org/10.1007/S10854-008-9595-3

30. Lakhera SK, Hafeez HY, Veluswamy P et al (2018) Enhanced photocatalytic degradation and hydrogen production activity of in situ grown TiO$_2$ coupled NiTiO$_3$ nanocomposites. Appl Surf Sci 449:790–798. https://doi.org/10.1016/j.apsusc.2018.02.136

31. Lopes KP, Cavalcante LS, Simões AZ et al (2009) NiTiO$_3$ powders obtained by polymeric precursor method: synthesis and characterization. J Alloys Compd 468:327–332. https://doi.org/10.1016/j.jallcom.2007.12.085

32. Li C, Li M (2002) UV Raman spectroscopic study on the phase transformation of ZrO$_2$, Y$_2$O$_3$-ZrO$_2$ and SO$_4{}^{2}$-/ZrO$_2$. J Raman Spectrosc 33:301–308. https://doi.org/10.1002/jrs.863

33. Al-Fatesh AS, Patel R, Srivastava VK et al (2022) Barium-promoted Yttria–Zirconia-supported Ni catalyst for hydrogen production via the Dry reforming of methane: role of barium in the phase stabilization of cubic ZrO$_2$. ACS Omega 7:16468–16483. https://doi.org/10.1021/acsomega.2c00471

34. Basahel SN, Ali TT, Mokhtar M, Narasimharao K (2015) Influence of crystal structure of nanosized ZrO$_2$ on photocatalytic degradation of methyl orange. Nanoscale Res Lett. https://doi.org/10.1186/s11671-015-0780-z

35. Al-Fatesh AS, Patel N, Srivastava V et al (2023) Iron-promoted zirconia-alumina supported Ni catalyst for highly efficient and cost-effective hydrogen production via dry reforming of methane. J Environ Sci. https://doi.org/10.1016/j.jes.2023.06.024

36. El-Salamony RA, Acharya K, Al-Fatesh AS et al (2023) Enhanced direct methanation of CO$_2$ using Ni-based catalysts supported on ZrO$_2$, CeO$_2$-ZrO$_2$, and La$_2$O$_3$-ZrO$_2$: the effect of support material on the reducible NiO-interacted species and catalytic activity. Mol Catal 547:113378. https://doi.org/10.1016/j.mcat.2023.113378

37. Al-Fatesh AS, Kumar R, Kasim SO et al (2022) Effect of cerium promoters on an MCM-41-supported nickel catalyst in dry reforming of methane. Ind Eng Chem Res 61:164–174. https://doi.org/10.1021/acs.iecr.1c03163

38. Al-Fatesh AS, Acharya K, Osman AI et al (2023) Rh promoted Ni over yttria–zirconia supported catalyst for hydrogen-rich syngas production through dry reforming of methane. Energy Sci Eng. https://doi.org/10.1002/ese3.1520

39. Fakeeha AH, Patel R, El Hassan N et al (2022) Holmium promoted yttria-zirconia supported Ni catalyst for H$_2$ production via dry reforming of methane. Int J Hydrogen Energy 47:38242–38257. https://doi.org/10.1016/j.ijhydene.2022.09.029

40. Al-Fatesh AS, Naeem MA, Fakeeha AH, Abasaeed AE (2014) Role of La$_2$O$_3$ as promoter and support in Ni/γ-Al$_2$O$_3$ catalysts for dry reforming of methane. Chin J Chem Eng 22:28–37. https://doi.org/10.1016/S1004-9541(14)60029-X

41. Kasim SO, Al-Fatesh AS, Ibrahim AA et al (2020) Impact of Ce-loading on Ni-catalyst supported over La$_2$O$_3$–ZrO$_2$ in methane reforming with CO$_2$. Int J Hydrogen Energy 45:33343–33351. https://doi.org/10.1016/j.ijhydene.2020.08.289

42. Fakeeha AH, Al-Fatesh AS, Srivastava VK et al (2023) Hydrogen production from gadolinium-promoted yttrium-zirconium-supported Ni catalysts through dry methane reforming. ACS Omega 8:22108–22120. https://doi.org/10.1021/acsomega.3c02229

43. Ferrari AC, Robertson J (2001) Resonant Raman spectroscopy of disordered, amorphous and diamondlike carbon. Phys Rev B Condens Matter Mater Phys 64:1–13. https://doi.org/10.1103/PhysRevB.64.075414

44. Cong C, Yu T, Saito R et al (2011) Second-order overtone and combination Raman modes of graphene layers in the range of 1690–2150 cm^{-1}. ACS Nano 5:1600–1605. https://doi.org/10.1021/nn200010m

45. Zou X, Li X, Gao X et al (2021) density functional theory and kinetic Monte Carlo simulation study the strong metal–support interaction of dry reforming of methane reaction over Ni based catalysts. Chin J Chem Eng 29:176–182. https://doi.org/10.1016/j.cjche.2020.05.009

46. Abd Ghani NA, Azapour A, Syed Muhammad AF, Abdullah B (2019) Dry reforming of methane for hydrogen production over Ni[sbnd]Co catalysts: effect of Nb[sbnd]Zr promoters. Int J Hydrogen Energy. https://doi.org/10.1016/j.ijhydene.2018.05.153

47. Kim H, Robertson AW, Kwon GH et al (2019) Biomass-derived nickel phosphide nanoparticles as a robust catalyst for hydrogen production by catalytic decomposition of C$_2$H$_2$ or dry reforming of CH$_4$. ACS Appl Energy Mater 2:8649–8658. https://doi.org/10.1021/acsaem.9b01599

48. Ibrahim AA, Fakeeha AH, Al-Fatesh AS (2014) Enhancing hydrogen production by dry reforming process with strontium promoter. Int J Hydrogen Energy 39:1680–1687. https://doi.org/10.1016/j.ijhydene.2013.11.050

49. Damyanova S, Shtereva I, Pawelec B et al (2020) Characterization of none and yttrium-modified Ni-based catalysts for dry reforming of methane. Appl Catal B Environ 278:119335. https://doi.org/10.1016/j.apcatb.2020.119335

50. Rahemi N, Haghighi M, Babaluo AA et al (2013) Non-thermal plasma assisted synthesis and physicochemical characterizations of Co and Cu doped Ni/Al$_2$O$_3$ nanocatalysts used for dry reforming of methane. Int J Hydrogen Energy 38:16048–16061. https://doi.org/10.1016/j.ijhydene.2013.08.084

51. Khatri J, Al-Fatesh AS, Fakeeha AH et al (2021) Ce promoted lanthana-zirconia supported Ni catalyst system: a ternary redox system for hydrogen production. Mol Catal 504:111498. https://doi.org/10.1016/j.mcat.2021.111498

52. Charisiou ND, Siakavelas G, Tzounis L et al (2018) An in depth investigation of deactivation through carbon formation during the biogas dry reforming reaction for Ni supported on modified with CeO_2 and La_2O_3 zirconia catalysts. Int J Hydrogen Energy 43:18955–18976. https://doi.org/10.1016/j.ijhydene.2018.08.074

53. Hu X, Jia X, Zhang X et al (2019) Improvement in the activity of Ni/ZrO_2 by cold plasma decomposition for dry reforming of methane. Catal Commun 128:105720. https://doi.org/10.1016/j.catcom.2019.105720

54. Pan C, Guo Z, Dai H et al (2020) Anti-sintering mesoporous Ni–Pd bimetallic catalysts for hydrogen production via dry reforming of methane. Int J Hydrogen Energy 45:16133–16143. https://doi.org/10.1016/j.ijhydene.2020.04.066

55. Mourhly A, Kacimi M, Halim M, Arsalane S (2020) New low cost mesoporous silica (MSN) as a promising support of Ni-catalysts for high-hydrogen generation via dry reforming of methane (DRM). Int J Hydrogen Energy 45:11449–11459. https://doi.org/10.1016/j.ijhydene.2018.05.093

56. Al-Fatesh AS, Chaudhary ML, Fakeeha AH et al (2021) Role of mixed oxides in hydrogen production through the dry reforming of methane over nickel catalysts supported on modified γ-al_2o_3. Processes 9:1–15. https://doi.org/10.3390/pr9010157

57. Al-Fatesh AS, Khatri J, Kumar R et al (2022) Role of Ca, Cr, Ga and Gd promotor over lanthana-zirconia–supported Ni catalyst towards H2-rich syngas production through dry reforming of methane. Energy Sci Eng 10:866–880. https://doi.org/10.1002/ese3.1063

58. Kumar P, Sun Y, Idem RO (2008) Comparative study of Ni-based mixed oxide catalyst for carbon dioxide reforming of methane. Energy Fuels 22:3575–3582. https://doi.org/10.1021/ef800326q

59. Chaudhary ML, Al-Fatesh AS, Kumar R et al (2022) Promotional effect of addition of ceria over yttria-zirconia supported Ni based catalyst system for hydrogen production through dry reforming of methane. Int J Hydrogen Energy 47:20838–20850. https://doi.org/10.1016/j.ijhydene.2022.04.199

60. Kurdi AN, Ibrahim AA, Al-Fatesh AS et al (2022) Hydrogen production from CO_2 reforming of methane using zirconia supported nickel catalyst. RSC Adv 12:10846–10854. https://doi.org/10.1039/d2ra00789d